

# Electromagnetic Sub-Wavelength Imaging Using Signal Processing Techniques Combined With Phase Conjugation

Xiang Gu, *Member, IEEE*, Chiara Pelletti, Raj Mittra, *Life Fellow, IEEE*, Yunhua Zhang, *Member, IEEE*

**Abstract**—In this paper, we show how we can combine Electromagnetics (EM) with signal processing algorithms to enhance the image resolution over that can be realized by using Electromagnetics techniques alone. We discuss several signal processing techniques, including the Correlation Method (CM) and the Minimum Residual Power Search Method (MRPSM), and apply them for sub-wavelength imaging in the microwave regime by combining them with the well-known Phase Conjugation (PC) algorithm, for instance, which has been extensively used in the electromagnetics area for imaging purposes. We show that by using this type of combination we can achieve sub-wavelength resolution on the order of  $\lambda_0/10$ , even if the measurement plane is not located in the very near-field region of the source. We describe the proposed imaging algorithms in detail and study their abilities to resolve at sub-wavelength level. We also study their computational efficiencies in a comparative manner.

**Index Terms**—Electromagnetics (EM), signal processing, sub-wavelength electromagnetic imaging, Phase Conjugation (PC), Correlation Method (CM), Minimum Residual Power Search Method (MRPSM)

## I. INTRODUCTION

THE concept of perfect lensing, performed by superlenses that are based on the use of negative refractive index materials, was introduced in [1], [2], and its potential for high resolution focusing rapidly attracted considerable attention. Recently, the topics of Phase Conjugation (PC), as well as Time Reversal Mirrors (TRM) [3]–[5] have been thoroughly investigated and a great deal of research has been conducted into optical sub-wavelength imaging [6], far-infrared near field imaging [7], resonant plasmonic

structures [8], as well as into electromagnetic sub-wavelength imaging [9]–[11].

Electromagnetic imaging with a resolution at the sub-wavelength level is attractive in many applications, which include high-directivity arrays used in modern self-tracking wireless communication systems [12], [13]; electromagnetic sounding of 3D structures of an inhomogeneous dielectric half-space for nanophysics, biological and medical diagnostics [14]; and short-range Ultra Wide Band (UWB) radar imaging [15], to name a few. Several approaches have been proposed for electromagnetic sub-wavelength imaging, including the use of left-handed materials [16], nonlinear metamaterial elements [17], array of parallel conducting wires [18], periodic layered metal-dielectric structures [19], metallic screens comprised of closely spaced and unequal slits [20], Fresnel zone-plates [21], Frequency Selective Surfaces (FSSs) [22], etc. A common feature of these techniques is that the image is formed in a plane located in the close proximity of the lens.

Some devices based on far-field phase conjugation have been reported, e.g., a phase conjugating lens consisting of a double-sided 2D assembly of straight wire elements [23], metallic strip gratings which perform evanescent-to-propagating wave conversion [24], sub-wavelength array of planar monopoles [25] and split-ring resonators loaded with varactor diodes [26]. The resolution capability of a phase conjugating lens has also been studied in [27], [28].

In this paper, we concentrate on the Fresnel region imaging capabilities of electromagnetics by combining it with signal processing algorithms. Section II discusses the Phase Conjugation technique, as well as its imaging capabilities. In Section III, two signal processing techniques, namely the Correlation Method (CM) and the Minimum Residual Power Search Method (MRPSM) are introduced and applied for sub-wavelength imaging in the microwave regime in conjunction with PC. We demonstrate that these signal processing algorithms can achieve sub-wavelength resolution even when the measurement plane is not located in the very near-field region of the source. The proposed algorithms are detailed below and their abilities to resolve at the sub-wavelength level are examined. In addition, their computational efficiencies are compared.

Manuscript received \*\*\*\*.

X. Gu is with the Electromagnetic Communication Laboratory, 319 Electrical Engineering East, Pennsylvania State University, University Park, PA 16802, and also with the Key Laboratory of Microwave Remote Sensing, Center for Space Science and Applied Research, Chinese Academy of Sciences, Beijing 100190, China (guxiang@mirslab.cn).

C. Pelletti and R. Mittra are with the Electromagnetic Communication Laboratory, 319 Electrical Engineering East, Pennsylvania State University, University Park, PA 16802 (chp13@psu.edu, mittra@engr.psu.edu).

Y. Zhang is with the Key Laboratory of Microwave Remote Sensing, Center for Space Science and Applied Research, Chinese Academy of Sciences, Beijing 100190, China (zhangyunhua@mirslab.cn).

## II. PHASE CONJUGATION

### A. Phase Conjugation (PC)

Algorithms for sub-wavelength imaging via PC are inspired by the principles of imaging lenses. Fig. 1 shows a representative scheme of 3D sub-wavelength imaging via PC. The test objects are assumed to be  $y$ -oriented PEC strips illuminated by a plane wave, that are located in the  $x$ - $y$  plane at  $z=0$ . The scattered field distribution is measured over a grid set up on the measurement plane at  $z=d$ , and then the measured data is phase conjugated and propagated to the image plane at  $z=2d$ , where an image of the original sources is obtained.

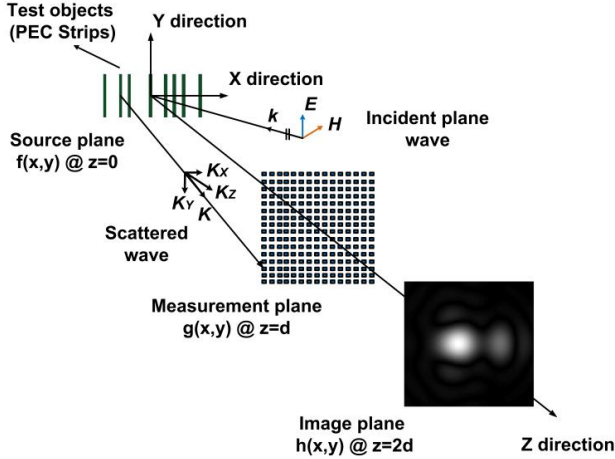


Fig. 1 Scheme for 3D sub-wavelength imaging via PC.

The Fourier transform [29] of the spatial field distribution over the  $x$ - $y$  plane located at  $z=0$  is expressed as:

$$F(k_x, k_y, z=0) = \int_{-\infty}^{\infty} \int_{-\infty}^{\infty} f(x, y, z=0) e^{jk_x x} e^{jk_y y} dx dy \quad (1)$$

where  $k_x$  and  $k_y$  denote the spectral variables;  $f(x, y, z=0)$  and  $F(k_x, k_y, z=0)$  represent the spatial and spectral distributions at the source plane, respectively.

The spectrum  $G(k_x, k_y, z=d)$  at the measurement plane can be derived, by propagating  $F(k_x, k_y, z=0)$  at a distance  $d$  along the  $z$ -direction, and using the relationship:

$$G(k_x, k_y, z=d) = F(k_x, k_y, z=0) e^{-jk_z d} \quad (2)$$

The wavenumber  $k_z$  in the  $z$ -direction is related to  $k_x, k_y$  and  $k_0$  ( $k_0 = 2\pi/\lambda_0$ ) as follows:

$$k_z = \begin{cases} \sqrt{k_0^2 - (k_x^2 + k_y^2)} & \text{when } k_x^2 + k_y^2 < k_0^2 \\ -j\sqrt{(k_x^2 + k_y^2) - k_0^2} & \text{when } k_x^2 + k_y^2 \geq k_0^2 \end{cases} \quad (3a)$$

$$(3b)$$

The form of  $k_z$ , as expressed by (3a), corresponds to the propagating waves (visible part of the spectrum), while (3b) defines the evanescent waves (invisible range of the spectrum).

The next step involves phase conjugating and propagating the spectrum  $G(k_x, k_y, z=d)$  to the image plane to derive  $H(k_x, k_y, z=2d)$ , and it is accomplished as shown below:

$$H(k_x, k_y, z=2d) = G^*(k_x, k_y, z=d) e^{-jk_z d} \quad (4)$$

After some simple manipulations, we obtain:

$$H(k_x, k_y, z=2d) = F^*(-k_x, -k_y, z=0) \quad (5)$$

which relates the spectrum at the image plane to that at the source plane.

After having performed the operations of Fourier transform, phase conjugation, and propagation to the image plane, we find that the spectrum at the image plane is a “flipped” (with respect to the spectral variables  $k_x$  and  $k_y$ ) and conjugated version of the original spectrum at the source plane.

By applying the well-known properties of the Fourier transform [30], the relationship between the spatial field distribution at the source and image planes can be expressed as follows:

$$h(x, y, z=2d) = f^*(x, y, z=0) \quad (6)$$

It is evident that the spatial field distribution at the image plane is the conjugate of the original spatial field distribution at the source plane.

The step-by-step procedure for imaging via PC can be summarized as follows:

- 1) Measure the  $E$ -field radiated from the sources at  $z=d$ .
- 2) Phase conjugate the spatial field distribution at  $z=d$ .
- 3) Fourier transform the spatial field distribution to the wavenumber domain at  $z=d$ .
- 4) Propagate the spectrum to the image plane at  $z=2d$ .
- 5) Take the inverse transform of the spectral distribution at  $z=2d$  to get the desired spatial image.

In general, if the phase conjugating lens is positioned in the far-field region of the sources, its resolution is always diffraction limited, because the evanescent component of the spectrum carrying sub-wavelength information cannot reach the phase-conjugating surface.

### B. Signal-to-Noise Ratio (SNR) Considerations

The underlying principle of phase conjugation is similar to that of a matched filter [31], which is an optimal linear filter for maximizing the Signal-to-Noise Ratio (SNR) in the presence of additive stochastic noise, by convolving the measured signal with a conjugated time-reversed version of the impulse response of the system. In the following, we study ways to enhance the performance of the PC algorithm by improving the SNR.

We begin with the measured data, obtained by sampling the scattered field in the measurement plane, and designate the power levels of the signal and noise to be  $P_S$  and  $P_N$ , respectively. The SNR of the measured data, represented as  $SNR_M$ , can then be written as  $SNR_M = P_S/P_N$ .

When we transform the measured data from the spatial to the wavenumber domain, the major portion of the signal power is concentrated in the visible region, defined by  $k_x^2 + k_y^2 < k_0^2$ , where  $k_0$  is the wavenumber of the excitation. This is true because the evanescent part of the spectrum, which is outside this region, decreases exponentially with the distance  $d$ . Hence, the information contained in the evanescent part of the spectrum decays rapidly when the

observation distance  $d$  is large. In the following discussion, the measurement plane is located  $5\lambda_0$  away; so we make an approximation that the information outside the visible region is damped to zero after propagating to a distance  $d$ . The noise power is distributed uniformly in the spectral domain, and we define  $P_N/S$  as the Power Density Distribution (PDD) of noise, where  $S$  represents the area of the spectral region:

$$S = (2\pi/dx)^2 \quad (7)$$

and  $dx$  is the spatial sampling rate in the  $x$ -direction at the measurement plane. We assume that the spatial sampling rates in the  $x$ - and  $y$ -directions are identical.

When we perform the PC, and then forward propagate the measured data to the image plane, the information beyond the region  $k_x^2 + k_y^2 < k_0^2$  is further attenuated. The corresponding attenuation coefficient of the noise power is defined as  $\alpha = \pi k_0^2 / S$ ; hence, we can express the SNR at the image plane, represented as  $SNR_I$ , as:

$$SNR_I = \frac{P_S}{\alpha \cdot P_N} = \frac{\lambda_0^2}{\pi(dx)^2} SNR_M \quad (8)$$

We can observe from (8) that  $SNR_I$  is considerably improved over  $SNR_M$ , by a factor expressed as:

$$\beta = \frac{\lambda_0^2}{\pi(dx)^2} \quad (9)$$

### C. Numerical Results

#### Effect of Observation Distance and Aperture Size

It is well known that if the scattered field distribution is measured in the vicinity of the source plane, a larger portion of the invisible information can be extracted from the measured data with no loss of visible information. However, the field distribution may be perturbed by the measurement probe if the probe is located in the proximity of the source. Hence, a far-field measurement is more desirable, even if this implies some loss of information of the invisible part of the spectrum.

Next, we investigate how the distance between the source and measurement planes, as well as the observation Aperture Size (AS) affects the resolution in the PC procedure.

For the sake of simplicity, but without loss of generality, we set the operating frequency to be  $1\text{GHz}$  and assume that the source is a  $y$ -oriented thin dipole with length  $15\text{cm}$ , i.e.,  $\lambda_0/2$ , located at the origin of the coordinate system at the source plane. The spatial sampling rate at the measurement plane is set to be  $3\text{cm}$ , i.e.,  $\lambda_0/10$ . Fig. 2 shows the spatial and spectral field distributions when the field is measured in the far-field zone, i.e.,  $150\text{cm}$  ( $5\lambda_0$ ) away from the source plane. The aperture size is increased from  $300\text{cm}$  to  $600\text{cm}$ , and then to  $900\text{cm}$ , both in the  $x$ - and  $y$ -directions; hence the size-to-distance ratio of the aperture  $R$ , defined as  $R = AS/d$ , first increases from 2 to 4, and then to 6.

Fig. 2(a) shows that the resolution is enhanced when AS is increased from  $300\text{cm}$  to  $600\text{cm}$ ; however, no substantial enhancement is observed as we increase AS from  $600\text{cm}$  to  $900\text{cm}$ . Fig. 2(b) shows that a larger portion of the

propagating part in the spectrum of the  $E_y$  at the measurement plane is retained when AS is increased from  $300\text{cm}$  to  $600\text{cm}$ ; however, the bandwidth of the propagating part in the spectrum, which has an inverse relationship with the resolution, is modified only slightly when AS is varied from  $600\text{cm}$  to  $900\text{cm}$ .

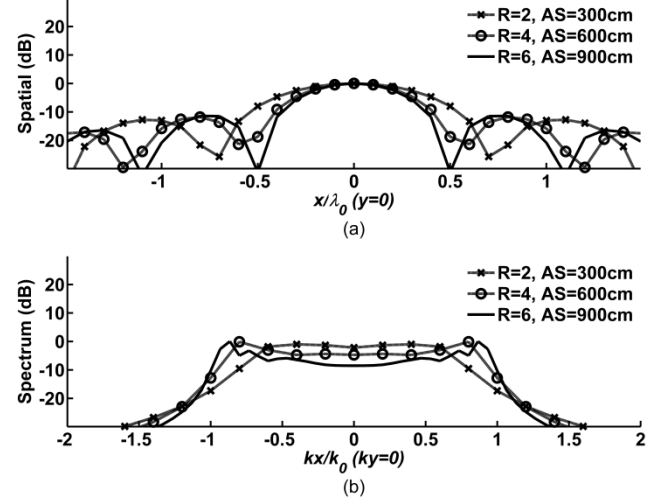


Fig. 2 (a) Normalized spatial distribution of  $E_y$  ( $y=0$  cut); and (b) normalized spectral distribution of  $E_y$  ( $k_y=0$  cut) at the image plane with different  $R$  and AS.

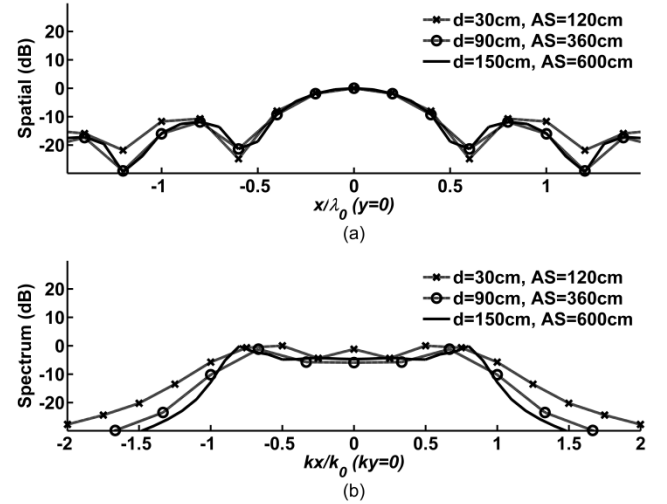


Fig. 3 (a) Normalized spatial distribution of  $E_y$  ( $y=0$  cut); and (b) normalized spectral distribution of  $E_y$  ( $k_y=0$  cut) at the image plane with different  $d$  and AS.

In Fig. 3, the size-to-distance ratio of the aperture,  $R$ , has been set to be 4 and has been kept unchanged. The distance  $d$  has been increased from  $30\text{cm}$  to  $90\text{cm}$ , and  $150\text{cm}$ , and AS has been increased from  $120\text{cm}$  to  $360\text{cm}$ , and  $600\text{cm}$ , respectively.

From Figs. 3(a) and 3(b), we see that regardless of the variations of  $d$  and AS, the resolution in the spatial domain, as well as the bandwidth in the spectral domain, have negligible effects when  $R$  is kept unchanged.

Not unexpectedly, as the distance  $d$  between the source and measurement planes is increased, a smaller portion of

the evanescent part of the spectrum reaches the measurement plane, and information originating from the source is transported there mainly via the propagating waves. This implies, in turn, that at the measurement plane, which is in the far-field zone of the sources, the maximum bandwidth of the spectrum is limited to  $2k_0$ . Thus, the highest resolution by using PC combined with the measurement in the far-field zone, cannot be smaller than  $\lambda_0/2$ . Hence, it is not possible to achieve sub-wavelength resolution if we rely solely on the PC algorithm.

Consequently, if we wish to improve the image resolution when the measurement plane is not in the near-field, we should increase the size-to-distance ratio of the aperture, keeping in mind that increasing this ratio beyond a certain level is not helpful for improving the resolution.

#### Enhancement of Signal-to-Noise Ratio

Next, we study the enhancement of the SNR from  $SNR_M$  (the SNR of the measured data at the measurement plane) to  $SNR_I$  (the SNR of the imaging data after phase conjugating at the image plane) when using the PC algorithm.

For the results presented in Table I, the operating frequency is set to be  $1\text{GHz}$ . The source is a y-oriented thin dipole whose length is  $15\text{cm}$ , located at the origin of the coordinate system at the source plane. The enhancement is investigated as a function of the distance, and the spatial sampling rate, as well as of different values of  $SNR_M$ .

Table I shows that  $SNR_I$  is definitely enhanced from  $SNR_M$  when we use the PC algorithm. Furthermore, the simulation results agree well with the theoretical results calculated by using Eq. (9).

TABLE I  
ENHANCEMENT ON SNR WHEN APPLYING PC

$d$ (cm)	$dx$ (cm)	$SNR_M$ (dB)	$SNR_I$ (dB)	Enhancement from simulation (dB)	Enhancement from Eq. (9) (dB)
30	10	10.00	14.19	4.19	4.57
30	10	20.00	24.21	4.21	4.57
30	6	10.00	18.62	8.62	9.01
30	6	20.00	28.64	8.64	9.01
150	10	10.00	14.50	4.50	4.57
150	10	20.00	24.50	4.50	4.57
150	6	10.00	18.93	8.93	9.01
150	6	20.00	28.93	8.93	9.01

From Table I, we observe that the difference between the simulation and theoretical results when  $d=150\text{cm}$  is approximately  $0.07\text{dB}$ , which is smaller than that when  $d=30\text{cm}$ , namely  $0.37\text{dB}$ . This can be attributed to the previously introduced approximation that the information outside the visible region is damped to zero after propagating to a distance  $d$ ; this is obviously more accurate when the observation distance is larger. Hence, the smaller difference is reasonable when  $d$  is set to be  $150\text{cm}$ .

Table I also shows that when the sampling interval is increased from  $6\text{cm}$  to  $10\text{cm}$ , the levels of enhancement reduce sharply, e.g., from  $9.01\text{dB}$  to  $4.57\text{dB}$ . This is due to the shrinkage of the area in the spectral domain, which is directly determined by the sampling interval.

For the case of different  $SNR_M$ , e.g.,  $10\text{dB}$  and  $20\text{dB}$ , the enhancements are the same. Thus, we note that the enhancement is not directly affected by  $SNR_M$ , but by the distance  $d$ , as well as by the sampling interval  $dx$ .

### III. CORRELATION METHOD AND MINIMUM RESIDUAL POWER SEARCH METHOD

#### A. Correlation Method (CM)

Next, we consider the problem of generating an image for an arbitrary combination of PEC strips, whose number is unknown as yet, and which have sub-wavelength separation distances. We begin by describing the correlation method (CM), which is widely used in signal processing, and explore the possibility of improving the image resolution by using this method.

The CM is based on correlating the field distribution generated by each of the assumed combinations of sources with the original one. The CM can be carried out at both the measurement and the image planes; and we will study the difference between these two in some detail.

The correlation coefficient is defined as:

$$\text{Corr.coef}(n) = \frac{1}{(M_i M_j - 1) \sigma_M \sigma_A} \sum_{i=1}^{M_i} \sum_{j=1}^{M_j} [(E^M(x_i, y_j) - \mu_M)(E_n^A(x_i, y_j) - \mu_A)^*] \quad (10)$$

where  $\mu_M$  and  $\mu_A$  represent the mean value of the field distribution of the assumed combinations of sources (subscript 'A') and the measured field ('M'), while  $\sigma_M$  and  $\sigma_A$  are their standard deviations, respectively.  $M_i$  and  $M_j$  are the numbers of samples along  $x$  and  $y$  gathered at the measurement plane.

We assume that an arbitrary number of PEC strips are present at the source plane, and that their number can vary from a single source to a predefined maximum number. For each of the generated combinations, we do the following: (i) compute the scattered field at the measurement plane and then correlate it with the measured data; or (ii) process both of them by PC and then correlate them at the image plane. The peak value of the correlation coefficient determines the correct position of the original sources at the source plane.

The CM can achieve a very high resolution if one can accurately locate the maximum correlation coefficient. However, the CM approach has some limitations of its own. First, the maximum correlation coefficient used to determine the correct source combination is only slightly larger than the one which is the next highest, especially when the sources are close to each other. Second, during the process of searching for the sources, the number of combinations to be considered can become very large and the computational burden can increase dramatically. For example, when the sources are randomly distributed in 10 positions, the number of combinations is  $2^{10}$ ; however, it rises to  $2^{40}$  when the source distribution involves 40 unknowns.

We can take advantage of the naturally independent characteristics of the CM, and use parallel computing

techniques [32] to reduce the computational burden. Moreover, we can further improve the computational efficiency of the parallel or distributed computations because the correlation operations with different combinations are totally independent and the communication between the processes is minimal. However, the cost of the hardware can be quite high if we follow this route, because if we assume that the combination is  $2^{40}$  and each processor is designed to calculate  $2^{20}$  combinations, the number of processor should be at least  $2^{20}$ , which is prohibitive. Hence, the CM approach is only suitable for application which the number of unknowns is moderate.

### B. Minimum Residual Power Search Method (MRPSM)

To circumvent some of the issues encountered earlier with the CM when the number of sources is not small, we apply the Minimum Residual Power Search Method (MRPSM), which systematically adjusts the local distribution of the sources by using an iterative minimum residual power search algorithm to obtain both the numbers and the positions of the sources.

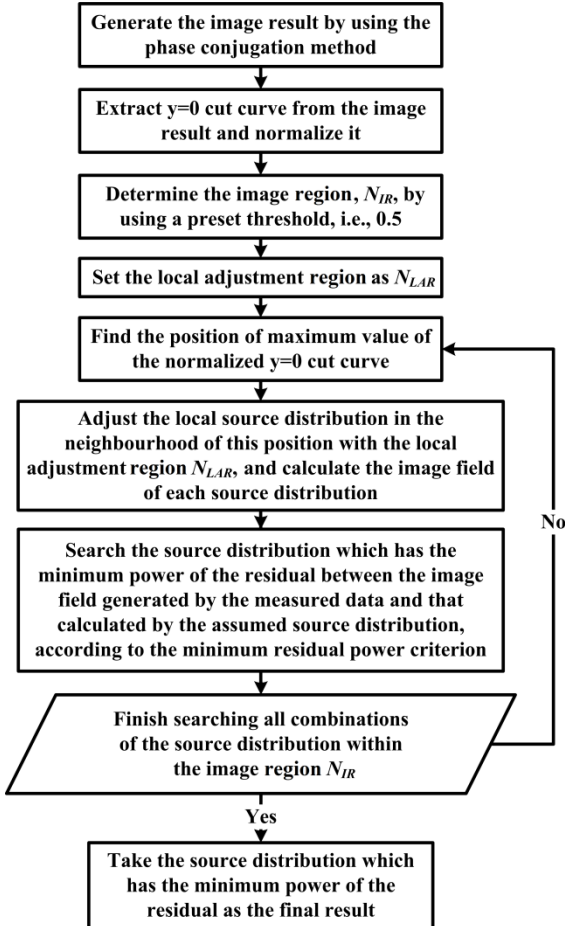


Fig. 4 Flow chart of MRPSM.

The step-by-step procedure for this method can be summarized as follows:

- 1) Generate the image result from the measurement data by using the PC method.

- 2) Extract the  $y=0$  cut from the image result and normalize the curve.
- 3) Determine the image region,  $N_{IR}$ , by using the criterion that this region only covers the locations where the level of the normalized field is higher than a preset threshold  $\delta V$ , e.g.,  $\delta V = 0.5$ .
- 4) Set the local adjustment region to be  $N_{LAR}$ .
- 5) Find the position of the maximum value of the normalized  $y=0$  cut curve.
- 6) Adjust the local source distribution in the neighborhood of this position with the local adjustment region  $N_{LAR}$ , and calculate the image field of each source distribution.
- 7) Search the source distribution which has the minimum power of the residual between the image field generated by the measured data and that calculated by the assumed source distribution, according to the Minimum Residual Power Criterion (MRPC).
- 8) Repeat until the search is finished and all the combinations of the source distribution within the image region  $N_{IR}$  have been considered.
- 9) Take the distribution which has the minimum power of the residual as the final result.

Fig. 4 shows the flow chart of the MRPSM.

The MRPC is defined as:

$$\Delta(n) = \min \left\{ \sum |E(x, y)|_n^2 - \sum |E(x, y)|_{measured}^2 \right\} \quad (11)$$

where  $\Delta(n)$  represent the power of the residual at the  $n$ -th search step.

### C. Numerical Model of the System of PEC Strips

As shown in Fig. 1, the sources are  $y$ -oriented identical PEC strips, whose length and width are  $15\text{cm}$  and  $1.5\text{cm}$ , respectively, and they are located along the  $x$ -direction at the source plane with a plane wave impinging on them.

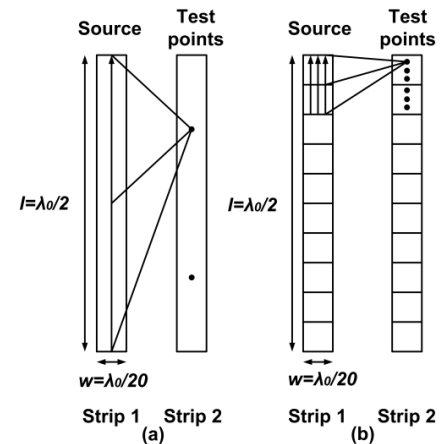


Fig. 5 Schematic representations of (a) SMBFs and (b) SRBFs.

In the CM and MRPSM approaches, we need to calculate the field distributions emanating from different combinations of these sources and then correlate or compare them to the measured field. To numerically model the current distribution over the sources, we employ either

the Sinusoidal MacroBasis Functions (SMBFs) [33]-[34], or the Sinusoidal Rooftop Basis Functions (SRBFs) [35].

As shown in Fig. 5, SMBFs assume that the induced surface current on the PEC strips is sinusoidal over the entire length of the dipole, while when using SRBFs, the current distribution is modeled as a superposition of sinusoidal rooftop type of basis functions. Typically, when using SRBFs, a half-wavelength strip is discretized into 10 and 3 sections in the  $x$ - and  $y$ -directions, respectively, which make the number of unknowns of the current distribution 27 times larger than that when we use the SMBFs method. However, SRBFs has much higher accuracy than SMBFs because of its more accurate current distribution model.

The impedance matrix elements can be computed by using one of the conventional numerical integration schemes [36]. Next, the weights of the current distribution are derived by imposing the tangential  $E$ -field to be zero on the surface of the strips, and then the  $E$ -fields are recomputed as in [35].

#### D. Numerical Results

##### Correlation Coefficient with Different SNR

In this section, we compare the properties of the CM before and after phase conjugation, as well as for different SNR values of the measured data.

The “measured” field data is derived by using FEKO 6.2 Suite [37]. The operating frequency is set to be 1 GHz, and the PEC strips are  $y$ -oriented, with length and width 15 cm and 1.5 cm, respectively. At the measurement plane, the sampling interval is 6 cm both in the  $x$ - and  $y$ -directions; while the corresponding number of samples is 101, so the aperture size is 600 cm. The distance  $d$  between the source and measurement planes is 150 cm.

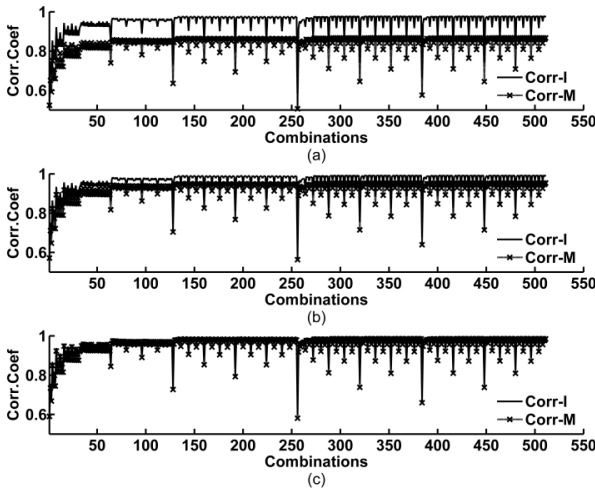


**Fig. 6** Correlation coefficients as a function of the combinations of the sources when (a)  $SNR_M = 5\text{ dB}$ , (b)  $SNR_M = 10\text{ dB}$ , and (c)  $SNR_M = 15\text{ dB}$ . The “Corr-M” and “Corr-I” represent the correlation coefficients by using the field at the measurement plane and the field at the image plane, respectively.

The 6 strips are located along the  $x$ -direction at  $(-12\text{ cm}, -9\text{ cm}, 0\text{ cm}, 3\text{ cm}, 6\text{ cm}, 12\text{ cm})$ , respectively. The minimum interval between the strips is 3 cm, i.e.,  $\lambda_0/10$ . We consider three cases:  $SNR_M = 5\text{ dB}$ ;  $SNR_M = 10\text{ dB}$ ;

and  $SNR_M = 15\text{ dB}$ . Without loss of generality, we use the SMBFs in the correlation operation because they offer higher computational efficiency.

Fig. 6(a)-(c) illustrate that the correlation coefficients (Corr-M) derived by correlating the originally measured field at the measurement plane obviously increase with the increasing of the  $SNR_M$ , from 5 dB to 10 dB, and then to 15 dB, while the correlation coefficients (Corr-I) derived by using the phase-conjugated field at the image plane increase only slightly. In addition, in Fig. 6(a), when  $SNR_M$  is 5 dB, the average difference between Corr-M and Corr-I is 0.11, while  $SNR_M$  is increased to 10 dB and 15 dB, the average differences decrease to 0.05 and 0.01, respectively. The reason is that the SNR at the image plane is improved over that at the measurement plane in the PC procedure. In fact, according to Eq. (9), this enhancement is approximately 9 dB.

In this simulation, we have set the threshold  $\delta V = 0.5$ , the image region contains 9 unknowns, i.e.,  $N_{IR} = 9$ , and the resulting number of combinations is 512.

##### Imaging Results

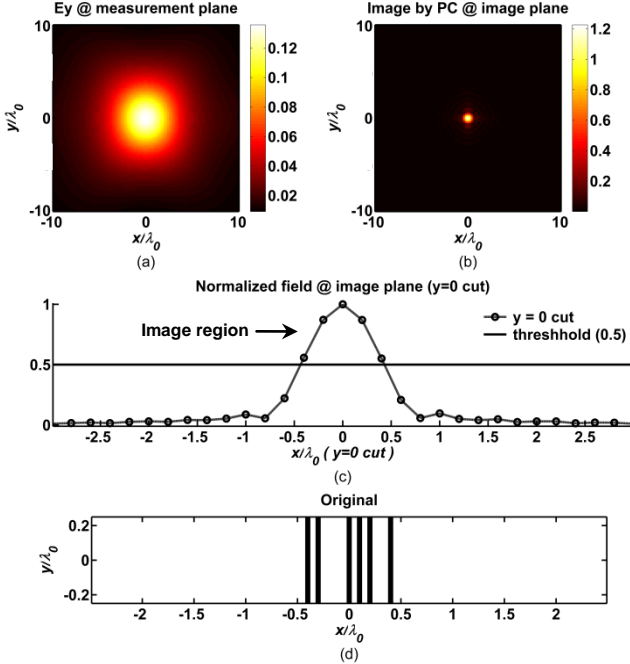
Numerical simulations of different distributions of PEC strips have been carried out by using the FEKO 6.2 Suite to generate the “measured” data. As described in Section II, the resolution obtained by using the PC on the field data measured in far-field zone can be improved by increasing the size-to-distance ratio of the aperture up to a certain value. However, due to physical constraints, the aperture size cannot be chosen as large as desired. In the following examples, we set the operating frequency to be 1 GHz, the distance between the source and measurement plane to be 150 cm, which is about  $5\lambda_0$ , and the observation aperture size to be 600 cm, implying that  $R = 4$ . The equivalent sources are  $y$ -oriented PEC strips, each with length 15 cm and width 1.5 cm, respectively. The sampling interval is 6 cm, both in the  $x$ - and  $y$ -directions, while the corresponding number of samples at the measurement plane is 101.

##### a. Case of 6 PEC Strips

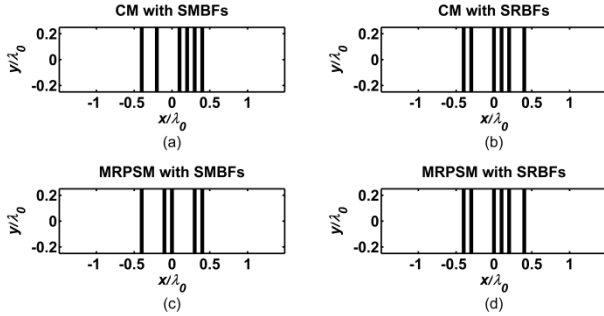
In this case, 6 PEC strips are located at the following  $x$  positions:  $(-12\text{ cm}, -9\text{ cm}, 0\text{ cm}, 3\text{ cm}, 6\text{ cm}, 12\text{ cm})$ , as shown in Fig. 7(d), and they are illuminated normally by a  $TE$ -polarized plane wave.

Fig. 7(a) shows the electric field distribution observed over an AS of  $20\lambda_0 \times 20\lambda_0$  at the measurement plane, and it is simulated by using FEKO. Fig. 7(b) shows the image generated by utilizing PC only, and it is apparent that this technique alone is unable to resolve the position of the sources, even though the maximum interval between the sources is  $0.3\lambda_0$ . Fig. 7(c) shows the  $y = 0$  cut of the normalized field distribution at the image plane. We set the threshold  $\delta V$  to be 0.5, and find that the region in the image plane where the values of the normalized field is above  $\delta V = 0.5$  ranges from  $-0.4\lambda_0$  to  $0.4\lambda_0$ . We set the unit interval to be  $0.1\lambda_0$ , so this image region contains 9 unknown units, implying that  $N_{IR} = 9$ . In the CM, the number of combinations is 512. In the MRPSM, we set  $N_{LAR}$  to be 9.





**Fig. 7** (a)  $E_y$  field distribution at the measurement plane; (b) image recovered by PCat the image plane; (c) normalized magnitude of  $E_y$  at the image plane ( $y=0$  cut) with a preset threshold, i.e., 0.5; and (d) original source distribution; black strips represent the PEC strips.



**Fig. 8** Recovered results by (a) CM with SMBFs; (b) CM with SRBFs; (c) MRPSM with SMBFs; and (d) MRPSM with SRBFs; black strips represent the PEC strips.

It can be seen from Fig. 8(a) and (c) that the results are not very accurate when we use SMBFs in the CM or MRPSM, although the SMBF method is 8 times faster. In contrast to this, it can be seen from Fig. 8(b) and (d) that the images are faithful reproductions of the object (array of strips) when we use SRBFs in the CM or MRPSM, albeit at an increased computational cost. The reason is that the SRBFs provide a better numerical representation of the current distribution over the strips.

#### b. Case of 15 PEC Strips

In this case, 15 PEC strips are located at the following  $x$  positions: (-60cm, -45cm, -30cm, -27cm, -24cm, -21cm, -18cm, 0cm, 9cm, 36cm, 39cm, 42cm, 45cm, 48cm, 60cm), respectively, as shown in Fig. 9(d).

These 15 PEC strips are illuminated by a  $TE$ -polarized plane wave, whose incidence angle is ( $\theta=45^\circ$ ,  $\varphi=0^\circ$ ). The

minimum separation distance between the strips is  $0.1\lambda_0$ . The image region is larger than  $4\lambda_0$ , as may be seen from Fig. 9(c); hence, the CM would not be as efficient in this case as it was in the previous example, even if we use parallel computing techniques to help reduce the computational burden to some extent. However, due to its inherent characteristics, the MRPSM is suitable for the case where the image region is wide, even though its computational complexity increases as we increase the width of the image region.

From the previous discussion, we see that the SMBFs have better efficiencies than the SRBFs, while the SRBFs have better accuracy in comparison to the SMBFs. In view of this, we propose a combination scheme, which begins with MRPSM with SMBFs for the initial estimation and follows this up with the final refinement by utilizing a combination of the MRPSM with SRBFs. Thus, combining the advantages of both the SMBFs and SRBFs methods, this approach can not only generate the primary results faster, but can also refine it to achieve a more accurate and reliable result with greater efficiency.

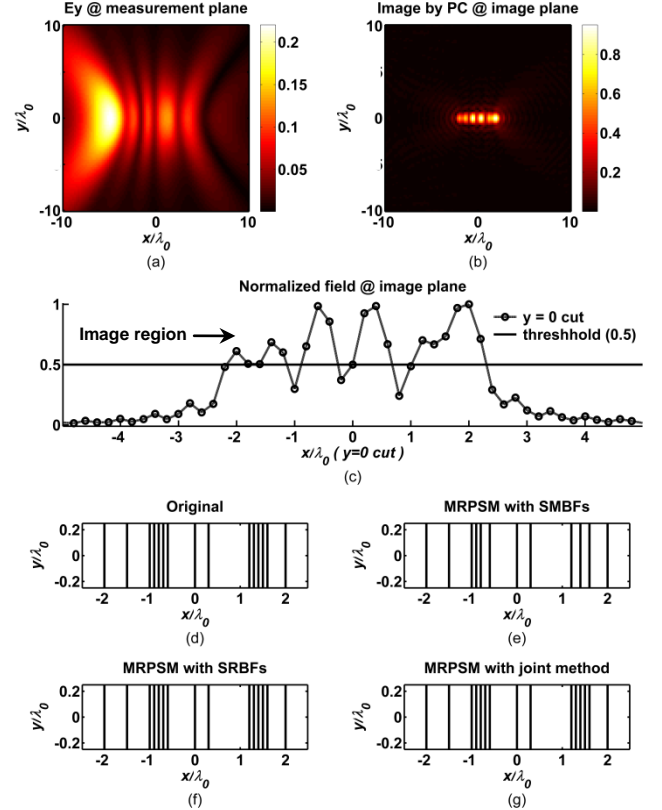


**Fig. 9** (a)  $E_y$  field distribution at the measurement plane; (b) image recovered by PC at the image plane; (c) normalized magnitude of  $E_y$  at the image plane ( $y=0$  cut); (d) original source distribution; and recovered results by (e) MRPSM with SMBFs, (f) MRPSM with SRBFs, and (g) MRPSM with joint method; black strips represent the PEC strips.

Fig. 9(a) shows the results for the simulated  $E_y$  field distribution derived by using FEKO, observed over an area of  $20\lambda_0 \times 20\lambda_0$  in the measurement plane. Fig. 9(b) shows the recovered image generated directly by utilizing the PC, and

it shows that the distribution of the source is comprised of several clusters. Fig. 9(c) shows the  $y=0$  cut of the normalized field distribution at the image plane, and the image region ranges from  $-2.2\lambda_0$  to  $2.3\lambda_0$  when we set the threshold  $\delta V$  to be 0.5. This image region contains 46 unknown units, i.e.,  $N_{IR}=46$ ; and we set  $N_{LAR}$  to be 9.

Fig 9(e) shows that the MRPSM applied by using the joint method generates a final recovered result, which is a faithful reproduction of the original distribution, as shown in Fig. 9(d). In addition, we compare the running times of the MRPSM with SMBFs, SRBFs, and joint method, and we find that the MRPSM with SMBFs is 6 times faster than that with SRBFs, and the MRPSM with joint method is 2 times faster than that with SRBFs. In conclusion, the MRPSM with SMBFs is the fastest, but it does not produce an accurate result. In contrast to this, the SRBFs and the joint method can recover the image results with good fidelity, though at an increased cost. In conclusion, the MRPSM offers good combination of efficiency and accuracy when combined with the joint method.

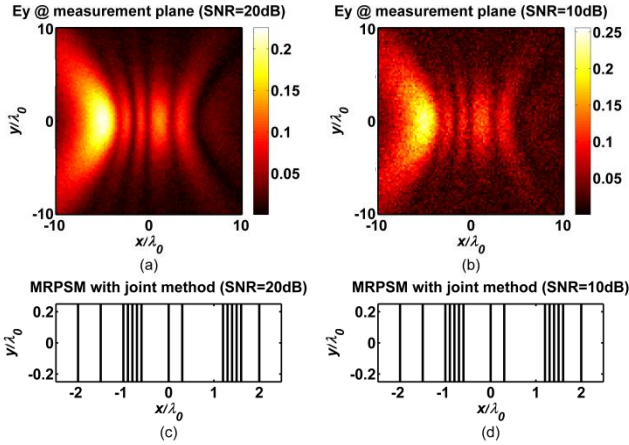


**Fig. 10**  $E_y$  field distribution at the measurement plane when (a)  $SNR_M = 20dB$ , (b)  $SNR_M = 10dB$ ; recovered results by MRPSM with joint method when (a)  $SNR_M = 20dB$ , (b)  $SNR_M = 10dB$ ; black strips represent the PEC strips.

Fig. 10 shows the numerical results for different levels of SNR of the measured data ( $SNR_M$ ). Fig. 10(a) and (b) show the  $E_y$  field distributions at the measurement plane with SNR to be 20dB and 10dB, respectively. Fig. 10(c) and (d) show the final estimations by using the MRPSM with joint method. It shows that this method can recover the correct positions of strips even when the SNR is 10dB; it also exhibits the robustness of the MRPSM with joint method.

Figs. 7-10 demonstrate that both the CM and the MRPSM can achieve a  $\lambda_0/10$  sub-wavelength resolution relatively efficiently when the image region is not wide. On the other hand, for the case when the image region is wide, the joint version of the MRPSM method, which combines the advantages of both SMBFs and SRBFs, produces accurate and reliable results with good efficiency. Specifically, such a joint approach can reliably achieve a sub-wavelength resolution of  $\lambda_0/10$  even when the image region is wide.

It is important to point out that in practice the local adjustment region  $N_{LAR}$  needs to be carefully chosen for a complex model. For instance, a large value of  $N_{LAR}$  may unnecessarily increase the computational complexity, while a value of  $N_{LAR}$  which is too small could reduce the accuracy of the results, because the mutual coupling effects may not be modeled sufficiently accurately.

#### IV. CONCLUSIONS

In this work, two signal processing techniques, namely the CM and MRPSM have been presented and their abilities to resolve at a sub-wavelength level, e.g.  $\lambda_0/10$ , have been examined. The methods, applied in the microwave regime, have been combined with the well-known PC method, to deal with the measured field in the Fresnel region of the source. We have described the proposed algorithms in detail, and have not only studied their abilities to resolve at the sub-wavelength level, but have also examined their computational efficiencies. These two algorithms can be easily extended to the case of more general source distributions, e.g., when the strips are not strung along a line. We believe that further research in this direction would be very fruitful, and it behooves us to pursue this avenue with vigor, rather than rely solely on electromagnetic imaging devices to achieve sub-wavelength resolution, by using lenses fabricated either with Double Negative (DNG) materials, or by using those containing active media.

#### APPENDIX I. LIST OF ACRONYM'S

CM: Correlation Method  
 MRPSM: Minimum Residual Power Search Method  
 PC: Phase Conjugation  
 TRM: Time Reversal Mirrors  
 UWB: Ultra Wide Band  
 FSS: Frequency Selective Surface  
 SNR: Signal-to-Noise Ratio  
 PDD: the Power Density Distribution of noise  
 $SNR_M$ : the SNR of the measured data at the measurement plane  
 $SNR_I$ : the SNR of the image field at the image plane  
 AS: Aperture Size in the measurement plane  
 MRPC: Minimum Residual Power Criterion  
 SMBF: the Sinusoidal Macro Basis Function  
 SRBF: the Sinusoidal Rooftop Basis Function  
 Corr-M: correlation coefficients derived by using the originally measured field at the measurement plane  
 Corr-I: correlation coefficients derived by using the phase conjugated field at the image plane  
 DNG: Double Negative materials

#### ACKNOWLEDGMENT

X. Gu and Y. Zhang acknowledge the financial support of the Chinese Academy of Sciences. The work was performed while X. Gu was a Visiting Scholar at the EMC Lab of the Pennsylvania State University



## REFERENCES

- [1] M. Nieto-Vesperinas, and E. Wolf, "Phase conjugation and symmetries with wave fields in free space containing evanescent components," *J. Opt. Soc. Amer.*, vol. 2, no. 9, pp. 1429–1434, 1985.
- [2] J. B. Pendry, "Negative refraction makes a perfect lens," *Phys. Rev. Lett.*, vol. 85, no. 18, pp. 3966–3969, 2000.
- [3] S. Maslovski, and S. Tretyakov, "Phase conjugation and perfect lensing," *J. Appl. Phys.*, vol. 94, no. 7, pp. 4241–4243, 2003.
- [4] A. Neice, "Methods and limitations of subwavelength imaging," *Adv. Imag. Elect. Phys.*, vol. 163, no. 18, pp. 117–140, 2010.
- [5] A.B. Katrich, "Do evanescent waves really exist in free space?" *Optics Communications*, vol. 255, no. 4-6, pp. 169–174, 2005.
- [6] Y. Ben-Aryeh, "Transmission enhancement by conversion of evanescent waves into propagating waves," *Appl. Phys. B*, vol. 91, no. 1, pp. 157–165, 2008.
- [7] S. Hunsche, M. Koch, I. Brener, and M. C. Nuss, "THz near-field imaging," *Optics Communications*, vol. 150, no. 1-6, pp. 22–26, 1998.
- [8] S. I. Maslovski, "Subwavelength imaging with arrays of plasmonic scatterers," *Optics Communications*, vol. 285, no. 16, pp. 3363–3367, 2012.
- [9] J. de Rosny, G. Lerosee, and M. Fink, "Theory of Electromagnetic Time-Reversal Mirrors," *IEEE Trans. Antennas Propag.*, vol. 58, no. 10, pp. 3139–3149, 2010.
- [10] R. Grimberg, A. Savin, and R. Steigmann, "Electromagnetic imaging using evanescent waves," *NDT&E International*, vol. 46, pp. 70–76, 2012.
- [11] V. Fusco, C. B. Soo, and N. Buchanan, "Analysis and characterization of PLL-based retrodirective array," *IEEE Trans. Microw. Theory Tech.*, vol. 53, no. 2, pp. 730–738, 2005.
- [12] J. de Rosny, and M. Fink, "Focusing properties of near-field time reversal," *Phys. Rev. A*, vol. 76, no. 6, pp. 065801–065801, 2007.
- [13] G. S. Shiroma, R. Y. Miyamoto, J. D. Roque, J. M. Cardenas, and W. A. Shiroma, "A high-directivity combined self-beam/null-steering array for secure point-to-point communications," *IEEE Trans. Microw. Theory Tech.*, vol. 55, no. 5, pp. 838–844, 2007.
- [14] K. P. Gaikovich, "Subsurface near-field scanning tomography," *Phys. Rev. Lett.*, vol. 98, no. 18, pp. 183902–183902, 2007.
- [15] I. Aliferis, T. Savelyev, M. J. Yedlin, J.-Y. Dauvignac, A. Yarovoy, C. Pichot, and L. Ligthart, "Comparison of the diffraction stack and time-reversal imaging algorithms applied to short-range UWB scattering data," *IEEE Int. Conf. Ultra-Wideband (ICUWB 2007)*, Singapore, Sep. 24–26, 2007.
- [16] N. Garcia, and M. Nieto-Vesperinas, "Left-handed materials do not make a perfect lens," *Phys. Rev. Lett.*, vol. 88, no. 20, pp. 207403–207403, 2002.
- [17] A. R. Katko, S. Gu, J. P. Barrett, B. -I. Popa, G. Shvets, and S. A. Cummer, "Phase conjugation and negative refraction using nonlinear active metamaterials," *Phys. Rev. Lett.*, vol. 105, no. 12, pp. 123905–123905, 2010.
- [18] P. A. Belov, Y. Hao, and S. Sudhakaran, "Sub-wavelength microwave imaging using an array of parallel conducting wires as a lens," *Phys. Rev. B*, vol. 73, no. 3, pp. 033108–033108, 2006.
- [19] P. A. Belov, and Y. Hao, "Sub-wavelength imaging at optical frequencies using a transmission device formed by a periodic layered metal-dielectric structure operating in the canalization regime," *Phys. Rev. B*, vol. 73, no. 11, pp. 113110–113110, 2006.
- [20] G. Eleftheriades, and A. Wong, "Holography-inspired screens for sub-wavelength focusing in the near field," *IEEE Microw. Wireless Compon. Lett.*, vol. 18, no. 4, pp. 236–238, 2008.
- [21] R. Merlin, "Radiationless electromagnetic interference: evanescent-field lenses and perfect focusing," *Science*, vol. 317, no. 5840, pp. 927–929, 2007.
- [22] O. Malyuskin, V. Fusco, and A. G. Schuchinsky, "Phase conjugating wire FSS lens," *IEEE Trans. Antennas Propag.*, vol. 54, no. 5, pp. 1399–1404, 2006.
- [23] O. Malyuskin, and V. Fusco, "Far field subwavelength source resolution using phase conjugating lens assisted with evanescent-to-propagating spectrum conversion," *IEEE Trans. Antennas Propag.*, vol. 58, no. 2, pp. 459–468, 2010.
- [24] M. Memarian, and G. V. Eleftheriades, "Evanescent-to-propagating wave conversion in sub-wavelength metal-strip gratings," *IEEE Trans. Microw. Theory Tech.*, vol. 60, no. 12, pp. 3893–3907, 2012.
- [25] G.-D. Ge, B.-Z. Wang, D. Wang, D. Zhao, and S. Ding, "Subwavelength array of planar monopoles with complementary split rings based on far-field time reversal," *IEEE Trans. Antennas Propag.*, vol. 59, no. 1, pp. 4345–4350, 2011.
- [26] A. R. Katko, G. Shvets, and S. A. Cummer, "Phase conjugation metamaterials: particle design and imaging experiments," *Journal of Optics*, vol. 14, no. 11, pp. 114003–114003, 2012.
- [27] V. F. Fusco, N. B. Buchanan, and O. Malyuskin, "Active phase conjugating lens with sub-wavelength resolution capability," *IEEE Trans. Antennas Propag.*, vol. 58, no. 3, pp. 798–808, 2010.
- [28] O. Malyuskin, and V. Fusco, "Imaging of dipole sources and transfer of modulated signals using phase conjugating lens techniques," *IET Microw. Antennas Propag.*, vol. 4, no. 8, pp. 1140–1148, 2010.
- [29] H. Chen, *Theory of Electromagnetic Waves*, New York: McGraw-Hill, 1983.
- [30] R. J. Beerends, *Fourier and Laplace transforms*, Cambridge University Press, 2003.
- [31] G. L. Turin, "An introduction to matched filters," *IRE Transactions on Information Theory*, vol. 6, no. 3, pp. 311–329, 1960.
- [32] Ricardo Corrêa, *Models for parallel and distributed computation: theory, algorithmic techniques and applications*, Kluwer Academic Publishers, 2002.
- [33] R. Mittra, C. Pelletti, N. L. Tsitsas, and G. Bianconi, "A new technique for efficient and accurate analysis of FSSs, EBGs and metamaterials," *Microwave and Optical Technology Letters*, vol. 54, no. 4, pp. 1108–1116, 2011.
- [34] C. A. Balanis, *Antenna Theory - Analysis and Design*, Third edition, John Wiley & Sons, 2005.
- [35] C. Pelletti, G. Bianconi, R. Mittra, A. Monorchio, and K. Panayappan, "Numerically efficient method-of-moments formulation valid over a wide frequency band including very low frequencies," *IET Microwaves, Antennas & Propagation*, vol. 6, no. 1, pp. 46–51, 2012.
- [36] E. C. Jordan and K. G. Balmain, *Electromagnetic Waves and Radiating Systems*, Prentice Hall of India, 2001.
- [37] FEKO Suite [Online]. Available: [www.feko.info](http://www.feko.info).